American Society of
Mechanical Engineers

ASME Accepted Manuscript Repository

Institutional Repository Cover Sheet

Christian Morsbach
First *Last*

ASME Paper Title: A Numerical Test Rig for Turbomachinery Flows Based on Large Eddy Simulations With a High-Order Discontinuous Galerkin Scheme - Part 3: Secondary Flow Effects

Authors: Christian Morsbach, Michael Bergmann, Adem Tosun, Bjoern F. Klose, Patrick Bechlars, Edmund Kuegeler

ASME Journal Title: Journal of Turbomachinery

Volume/Issue 146 (2) Date of Publication (VOR* Online) 13 November 2023

ASME Digital Collection URL: https://asmedigitalcollection.asme.org/turbomachinery/article/doi/10.1115/1.4063511/1167690/A-Numerical-Test-Rig-for-Turbomachinery-Flows

DOI: https://doi.org/10.1115/1.4063511

*VOR (version of record)

Christian Morsbach[1]
Institute of Propulsion Technology,
German Aerospace Center (DLR),
Linder Höhe, 51147 Cologne, Germany
email: christian.morsbach@dlr.de

Michael Bergmann
Institute of Propulsion Technology,
German Aerospace Center (DLR),
Linder Höhe, 51147 Cologne, Germany

Adem Tosun
Institute of Propulsion Technology,
German Aerospace Center (DLR),
Linder Höhe, 51147 Cologne, Germany

Bjoern F. Klose
Institute of Test and Simulation for Gas Turbines,
German Aerospace Center (DLR),
Linder Höhe, 51147 Cologne, Germany

Patrick Bechlars
MTU Aero Engines AG,
Dachauer Str. 665, 80995 Munich, Germany

Edmund Kügeler
Institute of Propulsion Technology,
German Aerospace Center (DLR),
Linder Höhe, 51147 Cologne, Germany

A Numerical Test Rig for Turbomachinery Flows Based on Large Eddy Simulations With a High-Order Discontinuous Galerkin Scheme - Part 3: Secondary Flow Effects

In this final paper of a three-part series, we apply the numerical test rig based on a high-order Discontinuous Galerkin scheme to the MTU T161 low pressure turbine with diverging end walls at off-design Reynolds number of 90,000, Mach number of 0.6 and inflow angle of 41°. The inflow end wall boundary layers are prescribed in accordance with the experiment. Validation of the setup is shown against recent numerical references and the corresponding experimental data. Additionally, we propose and conduct a purely numerical experiment with upstream bar wake generators at a Strouhal number of 1.25, which is well above what was possible in the experiment. We discuss the flow physics at midspan and in the end wall region and highlight the influence of the wakes from the upstream row on the complex secondary flow system using instantaneous flow visualization, phase averages and modal decomposition techniques.

Keywords: large eddy simulation, discontinuous Galerkin spectral element method, corner separation, unsteady wakes

1 Introduction

With the general reduction of core engine sizes, the importance of understanding and predicting losses generated by secondary flow effects is increasing. These effects have been reviewed in the literature for both compressors [1,2] and turbines [3] using predominantly experimental methods or, due to the computational expense, Reynolds-averaged Navier-Stokes (RANS) based numerical methods. While significant understanding has been established with these methods, new possibilities arise with the recent advances in scale-resolving simulations, such as Direct Numerical Simulation (DNS) or Large Eddy Simulation (LES). These reduce the uncertainty connected with RANS turbulence closures and can complement experimental campaigns with non-intrusive determination of the temporally and spatially highly resolved flow field. The majority of LES studies to date, however, has been limited to investigating the statistically two-dimensional flow of airfoil sections at midspan. Due to the increasing availability of computational resources and maturing of high-order LES methods, 3D simulations of low-pressure turbines (LPTs) including the effect of end wall boundary layers have become possible in recent years [4–10].

For example, Cui et al. [4] presented an extensive analysis of both midspan and end wall flow physics for the T106A LPT with parallel end walls at a Reynolds number of 160,000 using an incompressible second order accurate, unstructured Finite Volume (FV) method. The flow physics at midspan were illuminated using spanwise periodic simulations with and without incoming wakes at a reduced frequency of 0.68 based on chord length and trailing edge (TE) free stream velocity. In addition to the analysis of the suction side separation, they discussed the origin of longitudinal vortices on the pressure side as possible Görtler instability [11]. With simulations of the end wall flow resolving 40% of the span, they investigated the effect of the inflow boundary layer state (laminar or turbulent) on the development of the secondary flow system. Pichler et al. [6] investigated the effect of inflow boundary layer state on the secondary flows for the T106A at a Reynolds number of 120,000 and a Mach number of 0.59 using a compressible fourth order accurate Finite Difference (FD) method. The study was motivated by the scarce experimental data available about the incoming boundary layer and found that the shape of the velocity profile under constant boundary layer thickness has an influence on the extent of the secondary flow system into the passage. The midspan separation remained largely unaffected by this variation. A DNS analysis of the secondary flows in the T106A at a Reynolds number of 90,000 under the influence of wakes at a Strouhal number of 0.79 based on chord length and inflow axial velocity was conducted by Koschichow et al. [5] using an incompressible second order accurate FV solver. They showed only a weak influence of the wakes on the secondary flow system. It has to be noted, though, that the inlet boundary layer had a thickness of only 3% of the channel height. Another notable series of papers focuses on the front-loaded L2F LPT cascade at different Reynolds numbers employing state-of-the-art measurement techniques and numerical simulations with a compressible ninth order accurate FV solver with weighted essentially non-oscillatory (WENO) discretization [8,12]. Robison et al. [10] investigate the difference between wakes generated by bars compared to an LPT profile (50% reaction stage) at a Reynolds number of 160,000 and a Mach number of 0.1. While the bar wakes had very little influence on the secondary flows, the wake of the upstream blade did indeed suppress the secondary vortices in the passage due to its own strong secondary flow structures.

In this paper, we investigate the MTU T161, which is representative of high-lift LPT blades used in modern jet engines [13] and whose geometry and boundary conditions have been made pub-

[1]Corresponding Author.
Version 1.18, November 15, 2023

 Copyright © 2023 by ASME

Table 1 Overview of numerical setups. The number of degrees of freedom can be obtained by nDoF = $n_{xy} n_z (N+1)^3$.

Configuration	n_{xy}	n_z	nDoF / 10^6	nMPI	CPUh/t_c	$\Delta t/10^{-6} t_c$	t_{avg}/t_c	$\text{Ma}_{2,\text{th}}$	$\text{Re}_{2,\text{th}}$
Steady fine	5220	168	189.4	5120	25852	13.65	100	0.5963	89573
Steady coarse	3188	98	67.9	2560	5861	18.19	31	0.5974	89704
Steady unstructured	3696	168	134.1	2560	15324	13.65	64	0.5970	89644
Wakes unstructured	5385	168	195.4	1920	33712	13.02	78	0.5763	85873

licly available by MTU Aero Engines. In contrast to the literature discussed above, this case features end walls diverging at an angle of 12°. Iyer et al. [7] have performed a DNS of this cascade at the aerodynamic design point at a Reynolds number of 200,000 and a Mach number of 0.6 with laminar inflow boundary layer and no free stream turbulence using a compressible fifth order accurate flux reconstruction method. They present a thorough analysis of the midspan separation bubbles, which show a Kelvin-Helmholtz (KH) instability-based transition, and the end wall vortices. A DNS at a Reynolds number of 90,000 and a Mach number of 0.6 using a compressible second order accurate FV solver was conducted by Müller-Schindewolffs et al. [14] on a midspan section with slip walls to model the effect of the diverging end walls focusing on the modelling of the separation-induced transition on the suction side. Fard Afshar et al. [15] presented a full 3D LES of the same operating point using the compressible second order accurate FV scheme of our DLR Computational Fluid Dynamics (CFD) solver TRACE. Their analysis was focused on turbulence anisotropy in the transitional suction side region around midspan.

Our investigations are carried out using the high-order Discontinuous Galerkin (DG) solver of TRACE with sliding interface capability on unstructured hexahedral meshes [16,17]. For a detailed description of the numerical method, we refer the reader to part 1 of this paper. This study of the T161 is conducted at off-design conditions at an exit Mach number of 0.6, an exit Reynolds number of 90,000 and an inflow angle of 41°. The incoming end wall turbulent boundary layers and freestream turbulence are generated using a Fourier based synthetic turbulence generation method and carefully adjusted to reproduce the conditions found in the wind tunnel [18]. Both mid-span blade loading and the total pressure losses in a plane behind the blade will be shown to be in excellent agreement with the available experimental data [19] and recently published numerical data [15,20]. We assess the mesh independence of the results by comparing two structured grids with different resolutions and an unstructured hexahedral grid corresponding to the fine structured grid. Based on the validated setup, we use the extensive set of time-resolved data to analyze the flow physics starting with the statistically 2D phenomena encountered around blade mid-span. We then focus on the secondary flow structures and discuss them in view of existing literature.

Finally, we present a first application of the purely numerical test rig. Experiments with bar wake generators in the past have suffered from mechanical constraints preventing engine relevant Strouhal numbers and flow coefficients. Hence, we set up a full 3D configuration of the T161 with a cylindrical wake generator placed at a third of the axial chord length upstream of the blade and a Strouhal number 1.25. For a comparable average incidence angle on the blade, the inflow angle was adapted to account for the flow turning of the moving cylinder. We discuss the effect of the wakes on the average solution and investigate the involved mechanisms using phase-averages and modal decomposition techniques.

2 Numerical setup

Since the numerical method used in this paper itself has been extensively described in part 1, we restrain ourselves to the description of the numerical setup of the MTU T161 (see also [18]). We perform an implicit LES using a Discontinuous Galerkin Spectral Element Method (DGSEM) with Legendre-Gauss-Lobatto nodes and a polynomial order of $N = 5$ with anti-aliasing performed by the split-formulation of Kennedy and Gruber. Roe's approximate Riemann solver is applied for the advective part introducing sub-grid dissipation and the viscous terms are discretized by the Bassi-Rebay 1 scheme. To advance in time, a third-order explicit Runge-Kutta scheme of Shu et al. has been used. Turbulent fluctuations are introduced at the inflow plane using a Synthetic Turbulence Generator (STG) based on a superposition of Fourier modes with random phases and direction vectors, which produce a modified von Karman spectrum [21].

An overview of all computations presented here is given in Tab. 1. The isentropic Mach number $\text{Ma}_{2,\text{th}}$ is obtained from the isentropic relation between the inlet total pressure $p_{t1,\text{ref}}$ and the outlet static pressure $p_{2,\text{ref}}$. With the inlet total temperature $T_{t1,\text{ref}}$ and the chord length C, the isentropic Reynolds number $\text{Re}_{2,\text{th}}$ can be obtained using Sutherland's law for the viscosity. We define a convective time unit $t_c = C/||\overline{\mathbf{u}_{2,\text{area}}}||$ using the chord length and the area averaged outlet velocity. Note, that some authors define this based on axial chord length and axial outlet velocity which would result in $2.13 t_c$ for this case. The bar passing period is given by $t_{\text{bar}} = l_{\text{pitch}}/u_{\text{bar}} = 1.554 t_c$. Hence, the averaging time for the simulation with wakes covers 50 bar passes. All LES were initialized with RANS solutions and run for roughly $10 t_c$ to wash out the initial transient before starting to record statistics. The end of the initial transient was confirmed using the marginal standard error rule (MSER). The method analyzes the reduction of the statistical confidence interval on the mean for a given quantity by using an increasing number of samples going backwards through the time signal. It then marks the end of the initial transient as the time where the confidence interval becomes minimal. A detailed description this method applied to the LES of an LPT can be found in [22].

All computations were conducted on DLR's CARA HPC cluster consisting of compute nodes with two AMD EPYC 7601 (32 cores; 2.2 GHz) CPUs and 128 GB DDR4 RAM each, connected via InfiniBand HDR. Note that none of these simulations were conducted in a clean environment required to produce reliable performance and scaling results. As discussed in part 1 of this paper, the parallel efficiency of the sliding mesh interface can be improved in the future by introducing restrictions on the mesh topology at the interface.

2.1 Meshing strategy. The DGSEM employed in this work [17] requires conformal meshes consisting of hexahedra only. Furthermore, the elements need to have a geometry order greater than one to allow for the representation of smoothly curved boundaries. One of the great advantages of this method is the fact, that it allows for unstructured grids. However, mesh generation tools capable of creating conformal pure hexahedral meshes with unstructured 3D refinement/coarsening are not readily available. In 2D, on the other hand, reliable algorithms exist to create conformal pure quadrilateral meshes, which are implemented in the open source software Gmsh [23]. This leads to our current meshing strategy for prismatic blades. We first create a 2D pure quadrilateral mesh either with a block structured or fully unstructured topology. In a second step, it is extruded using an S2m grid, which essentially contains the relationship of axial position and spanwise point distribution, to obtain the final pure hexahedral mesh. This approach comes with the limitation, that the wall-parallel resolution required at hub and tip is fixed for all

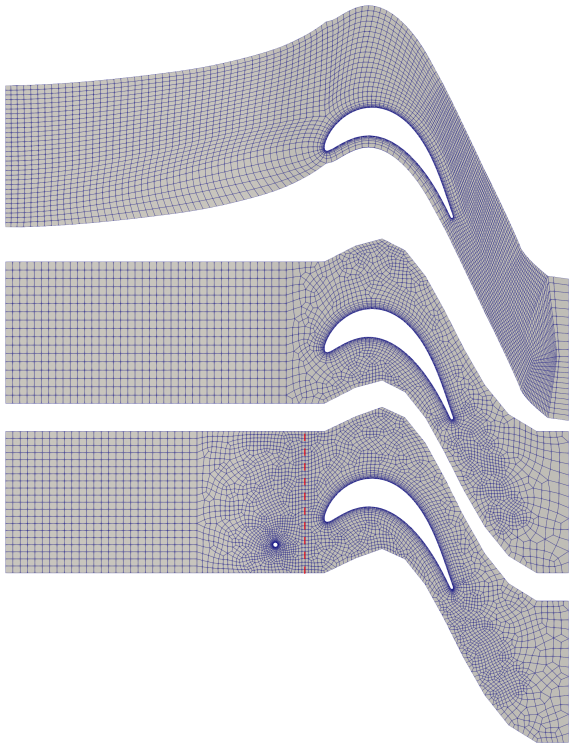

Fig. 1 High-order grids in xy-plane (inner solution points not shown) for cases steady fine (*top*), steady unstructured (*middle*) and wakes unstructured at phase $\phi = 0$ with sliding interface in red (*bottom*)

spanwise planes.

Fig. 1 shows the different 2D grid topologies used to simulate the flow through the cascade. Only the high-order elements without their inner solution points are shown. The first (*top*) is a block structured grid topology which has been used in previous studies, e.g. [17,24], created with our in-house tool PyMesh. Both the fine and the coarse mesh use this topology. It consists of an O-block around the blade to accurately represent the boundary layers. It is wrapped by a C-block and the remaining space is filled with H-blocks. This topology allows for a high-quality mesh in terms of stretching rates and orthogonality. A major drawback here is, that changes in resolution in one part of the domain often affect large portions of the mesh. Hence, trying to fulfill minimum resolution requirements almost automatically leads to excessive resolution in other parts of the domain.

This problem can, of course, be overcome by a fully unstructured topology (*middle*). Here, we start with a boundary layer mesh of O-type as well, with the difference, that now the points around the blade can be distributed freely without any topological restrictions. High resolution in the wake is enforced locally without effect on any other region of the domain. Towards the outflow, the resolution can be easily relaxed. Towards the inflow boundary, on the other hand, we introduce a transfinite block as in the block structured case to ensure a high-quality mesh for the incoming turbulence. Compared to the block structured case, we were able to reduce the number of elements per plane n_{xy} by 29% (see Tab. 1) using this approach while enforcing the same LES resolution requirements with respect to the end wall boundary layer and even improving the resolution on the pressure side (see Fig. 2).

Finally, Fig. 1 (*bottom*) shows the unstructured grid with the wake generator placed upstream of the blade. Here, the blade mesh was kept and only the region around the wake generator was newly designed. A small but important detail is the introduction of one layer of transfinite elements upstream and downstream of the sliding interface shown as dashed red line. This ensures that

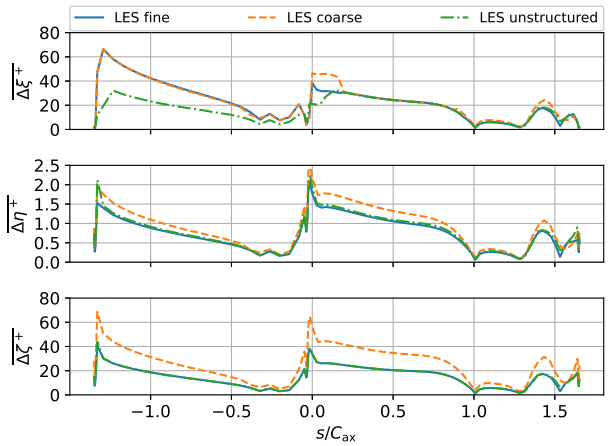

Fig. 2 Midspan non-dimensional cell sizes for the steady cases

elements connect with the interface with their faces, not with edges only. The mesh around the wake generator increases the number of elements by 47% compared to the steady case.

Sufficient grid resolution has to be verified for LES. This can be done by comparing average solution point distances, defined as element edge length divided by polynomial order N, in wall units. In Fig. 2, these are given as $\overline{\Delta\xi^+}$ (streamwise), $\overline{\Delta\eta^+}$ (wall normal) and $\overline{\Delta\zeta^+}$ (spanwise) on the blade centerline. The major issue with the coarse mesh was the spanwise resolution. It was fixed by approximately doubling the number of elements in spanwise direction in the fine mesh. Additionally, the wall normal spacings were slightly reduced. The unstructured mesh was designed to essentially replicate the properties of the fine mesh on the suction side while the unstructured topology could be exploited on the pressure side to significantly increase the streamwise resolution locally. On the end walls, cell sizes in streamwise and spanwise cell direction have to be taken as approximate since the cells are not perfectly aligned with the flow direction for the structured mesh. For the fine mesh, streamwise, wall normal and spanwise resolution of $\overline{\Delta\xi^+}, \overline{\Delta\eta^+}, \overline{\Delta\zeta^+}) < (65, 1.7, 60)$ was achieved with average values of $(23, 0.81, 19)$. Since the construction of the unstructured mesh followed the structured one, the same maxima were enforced, allowing slightly larger average values. The resolution in the free stream was ensured by the ratio of solution point distance and estimated Kolmogorov scale below 6 along a mid passage streamline. In Sec. 3, results for all three different grids will be shown to assess the mesh influence on different aspects of the flow.

2.2 Synthetic turbulence. The procedure to derive appropriate inflow boundary conditions both in terms of boundary layer development and freestream turbulence decay has been recently described by the present authors [18]. We repeat the most important aspects here. A preliminary finite length channel flow is simulated using the same mesh and flow conditions as in the planned simulations of the cascade. For this, we choose a boundary layer profile from a DNS database [25], whose momentum thickness Reynolds number is lower than our target known from the experiment, and scale it to match the desired freestream total pressure. Outside of the boundary layer, we set a first guess of Reynolds stresses and turbulent length scale. From the resulting development of boundary layer thickness, we can deduce the required distance of the inlet plane from the upstream measurement position for the cascade simulation. Once, the position of the inlet plane is fixed, the freestream turbulence quantities can be adapted to achieve the required decay. It has to be noted in this case, that we chose a stronger decay than seen in the experiment to avoid

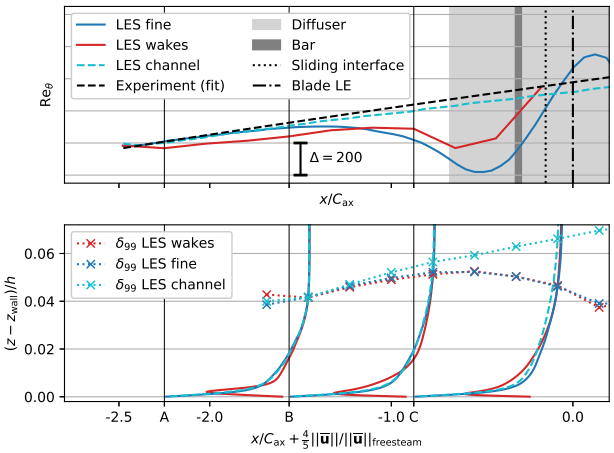

Fig. 3 Development of inflow boundary layer momentum thickness Reynolds number Re_θ and normalized boundary layer profiles at selected axial positions A, B and C, δ_{99} boundary layer edge illustrated in lower plot

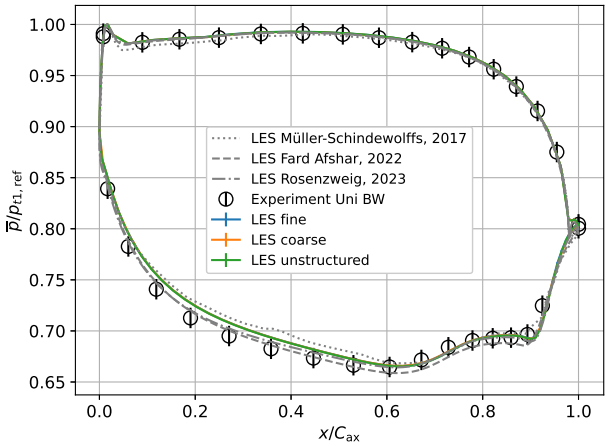

Fig. 4 Midspan relative blade pressure compared with numerical results of Müller-Schindewolffs [14], Fard Afshar [15], Rosenzweig [20] and experiments [19]

a turbulent length scale so large that it conflicts with the periodic boundaries. So, while we match the development of the boundary layer thickness, we only match the turbulence intensity at the leading edge (LE) of the blade [18].

Fig. 3 shows the result of this procedure in terms of momentum thickness Reynolds number Re_θ and selected boundary layer profiles (A, B, C) for the channel flow compared with both LES setups and experimental data. The experimental setup corresponds to the clean channel flow with parallel end walls since the cascade was not installed in the rig for these measurements. The geometrical features of the LES setup with diverging end walls and the blade are illustrated for orientation. While the boundary layer at stations A and B shows good agreement between the channel flow and the setup with blade, the combined upstream effect of the blade and diffuser can be observed at station C. Note that our δ_{99}/h boundary layer thickness falls between values from literature of roughly 0.01 [4] and 0.1 [6] (both determined by optical inspection of their velocity plots).

2.3 Wake generators. We chose a circular cylinder with a diameter of $d_{\mathrm{bar}} = 2$mm to investigate the effect of unsteady wakes on the cascade flow and see this only as a first step towards full blade row interaction studies. In contrast to a full upstream turbine blade, the cylinders will not generate pronounced secondary flows at the end wall, which would have different effects on the downstream blade row [10]. Compared to the experiment, we are able to achieve more realistic flow coefficients and Strouhal numbers because the simulation does not suffer from mechanical constraints of the thin cylinder. One wake generator per cascade blade is placed at an axial distance of $0.3C_{\mathrm{ax}}$ upstream of the LE resulting in a flow coefficient of $\Phi = u_{1,\mathrm{ax}}/u_{\mathrm{bar}} = 0.78$ based on the pitch-averaged centerline axial velocity between the bar and the blade LE at $x/C_{\mathrm{ax}} = -0.2$ and a Strouhal number of

$$\mathrm{Sr} = \frac{C_{\mathrm{ax}} u_{\mathrm{bar}}}{l_{\mathrm{pitch}} u_{2,\mathrm{is,ax}}} = 1.25 \tag{1}$$

with the centerline isentropic axial exit velocity $u_{2,\mathrm{is,ax}}$ computed from the isentropic exit Mach number, outflow angle and outflow speed of sound.

A cylinder moving through a uniform flow will produce both total pressure loss and flow turning. The first, if not corrected for, leads to a slight reduction in isentropic Reynolds and Mach number as shown in Tab. 1. The second, more importantly, will change the effective incidence for the blade. To be able to discuss the effects of upstream wakes independently, we adapted the flow angle at the inlet of the domain such that the blade sees the same averaged incidence of 41° as in the steady case. After a series of first RANS and then LES of only a spanwise periodic moving circular cylinder, the inflow angle was set to be $\alpha_1 = 47°$. The usage of LES in this prestudy was necessary because RANS cannot accurately predict cylinder drag.

The end walls are moving at the same relative velocity as the cylinder from the inlet up to $x/C_{\mathrm{ax}} = -0.15$. Nevertheless, we specify the same boundary layer profile at the inflow. As a result, the end wall boundary layers will be skewed due to the viscous forces and experience a sudden change in wall velocity just upstream of the blade. This setup is comparable to the procedures in multi-stage RANS when cavities are not resolved. Fig. 3 shows the resulting reduction in Re_θ and the effect on the boundary layer profiles in the absolute frame of reference. In contrast to the simulations with non-moving end walls, the absolute velocity at the wall non-zero for the case with wakes. From station A to C it can be seen how the diffusion of momentum towards the channel center deforms the velocity profile. Overall, the integral parameters of the boundary layer are still comparable and smaller than the variation investigated by Rosenzweig et al. [20].

3 Verification

Before we start to analyze the influence of wakes, we will verify our setup without wake generators against experimental data and other numerical studies of the same or a very similar configuration. It is important to clearly state how the non-dimensionalization of the shown quantities has been performed. We need a reference stagnation temperature, stagnation pressure and static pressure, which we choose to determine in the following way. The reference stagnation temperature $T_{t1,\mathrm{ref}}$ and pressure $p_{t1,\mathrm{ref}}$ are chosen as the maximum values of the temporally averaged centerline temperature and pressure distribution on the blade surface. The reference static pressure $p_{2,\mathrm{ref}}$ is taken as the time and pitchwise area averaged pressure in the outflow plane at $x/C_{\mathrm{ax}} = 1.914$. With these quantities and the chord length C of the blade, we can compute the isentropic Mach and Reynolds numbers using the isentropic relations and Sutherland's law for the viscosity. Tab. 1 confirms that the intended operating point has been successfully set up.

The midspan blade loading is shown in Fig. 4 against experimental [19] and numerical [14,15,20] references as relative pressure $p/p_{t1,\mathrm{ref}}$. The error bars for the experimental data indicate an estimated 1%-point uncertainty for the pressure measurements for orientation. For the numerical references, there is no information

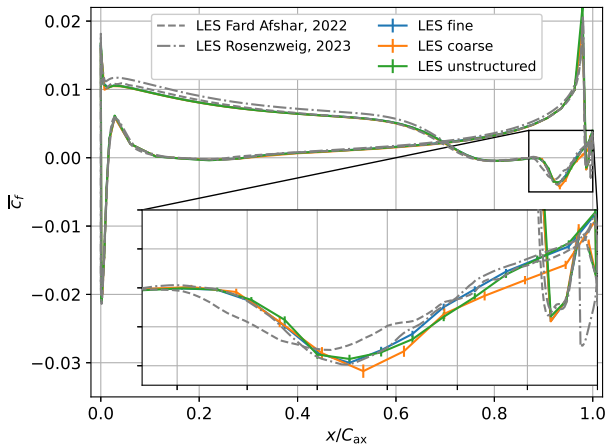

Fig. 5 Midspan blade skin friction coefficient

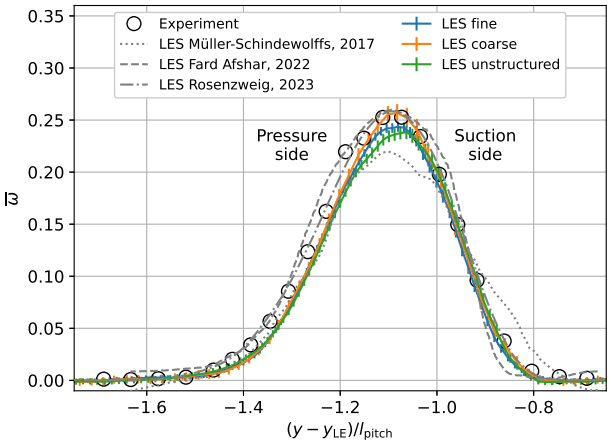

Fig. 6 Midspan wake total pressure loss coefficient at $x/C_{ax} = 1.4$

available on sampling error. In the following, we will show 68% confidence intervals for all our LES runs [22]. In this figure, they are within the line thickness for this rapidly converging quantity. First of all, the mesh dependence for this quantity is negligible for the three setups considered here. Our results show excellent agreement with the experiments and the other LES on the pressure side. Only in the region on the suction side leading up to separation, there is a slight offset between experiment and numerics and also some scatter between the different numerical references. This offset can also be seen in Fig. 5 compared to Rosenzweig's results for the skin friction coefficient computed as

$$\overline{c_f} = \frac{\mathrm{sgn}(\overline{\tau_{w,x}})\sqrt{\overline{\tau_{w,x}}^2 + \overline{\tau_{w,y}}^2}}{p_{t1,\mathrm{ref}} - p_{2,\mathrm{ref}}}. \tag{2}$$

Apart from that, subtle differences between the numerical results are only apparent in the transition and reattachment region shown in the zoomed inset axes. Compared to our and Rosenzweig's results, Fard Afshar obtained a slightly premature transition peak. Furthermore, our coarse mesh shows a slightly delayed recovery after reattachment.

The turbulent mixing behind the blade is another important aspect of the flow. We evaluate the total pressure loss coefficient

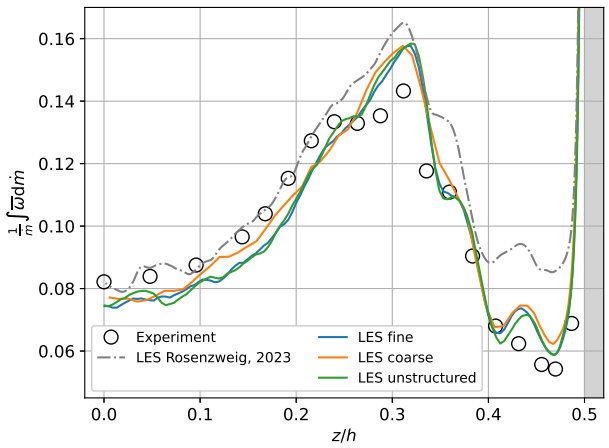

Fig. 7 Pitch averaged wake total pressure loss coefficient at $x/C_{ax} = 1.4$

$$\overline{\omega} = \frac{p_{t1,\mathrm{ref}} - p_t(\overline{\rho}, \overline{u}, \overline{v}, \overline{w}, \overline{p})}{p_{t1,\mathrm{ref}} - p_{2,\mathrm{ref}}}, \tag{3}$$

where we compute the local stagnation pressure p_t from the time-averaged primitive variables via the isentropic relations for an ideal gas, in the plane at $x/C_{ax} = 1.4$. Fig. 6 shows ω at midspan in the blade-to-blade direction. All reference results have been offset along the y-axis to align with the peak loss, since the exact coordinate system was not known. Again, the agreement with the experiments and the 3D LES results is satisfactory. The Q3D result by Müller-Schindewolffs [14] deviates both in terms of peak loss and of the slope on the suction side.

As a final verification, Fig. 7 shows the pitchwise mass averaged total pressure loss coefficient over the relative channel height in the same plane. Here, the upper and the lower half of the channel have been used for a combined average by exploiting the symmetry about the midspan plane. Apart from the consistent offset to Rosenzweig's results (profile B) [20] from midspan to about $x/h = 0.3$, the major difference between can be seen close to the end wall for $x/h > 0.4$. Our results show better agreement with the measured data in this region, although both inflow boundary layer profiles share the same momentum thickness. The discrepancy might be attributed to differences in the boundary layer thickness δ_{99} and will be investigated in the future.

In summary, two conclusions can be drawn. Our setup is consistent with both the experiment and recent numerical simulations with different discretization schemes. For the quantities shown in the above discussion, we have used sufficient grid resolution as the differences between our three simulations are mostly within the 68% confidence intervals. We have identified a region in the reattaching flow at midspan where the coarse mesh shows some deviation. However, the two topologically different grids (fine and unstructured) show excellent agreement in all respects. Hence, we see our setup as sufficiently verified to continue with a more detailed analysis of the flow physics.

4 Flow analysis

Fig. 8 gives an impression of the instantaneous turbulent structures for both cases. In the following, we will discuss the flow physics focusing first on the suction and then on the pressure side.

4.1 Suction side. We start our discussion of the flow physics with a midspan section of the blade, which is essentially not influenced by the secondary flow structures. On average, the flow separates on both the suction and pressure side of the blade as can

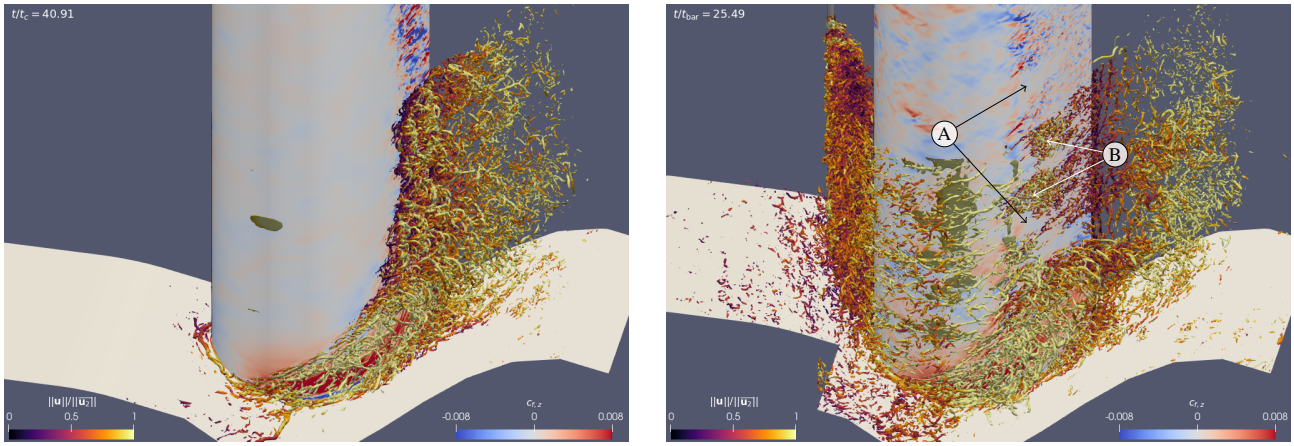

Fig. 8 Instantaneous vortex structures of the flow through the MTU T161 LPT visualized by a $QC_{ax}^2/||\overline{u_2}||^2 = 500$ isosurface clipped at midspan for the case without wakes (*left*) and with wakes (*right*)

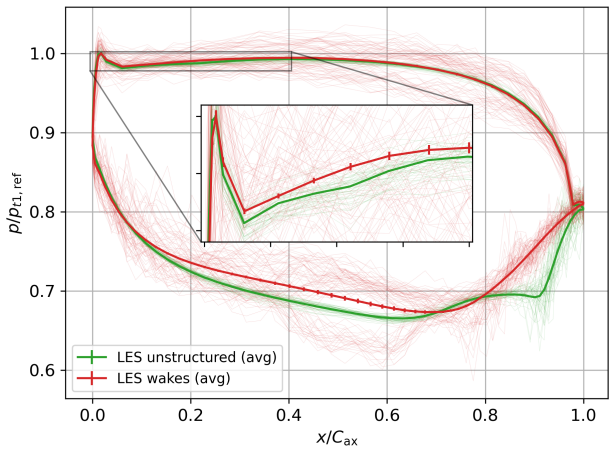

Fig. 9 Comparison between cases with and without wakes of midspan relative blade pressure with instantaneous values as thin lines

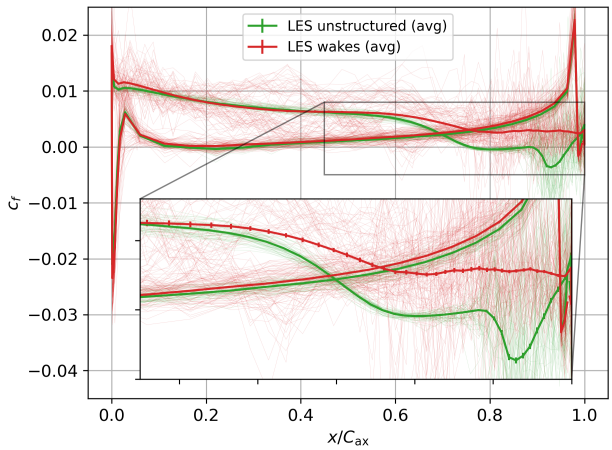

Fig. 10 Comparison between cases with and without wakes of midspan blade skin friction coefficient with instantaneous values as thin lines

be seen in Fig. 9 and 10. In addition to the average values, instantaneous values are shown as thin lines to give an indication of the variance. A classic laminar separation bubble with subsequent transition to turbulence in the separated shear layer can be observed on the suction side. This follows the Kelvin-Helmholtz instability mechanism as already discussed in the literature [7,14,15]. The turbulent wakes are able to completely suppress the separation on average. However, the instantaneous vorticity in Fig. 11 and the phase-averaged surface streaklines in Fig. 12 show intermittent separation for $\phi = 0.4$ and 0.6 (A). As can be seen in Fig. 8 (*right*), there is a strong spanwise variation in the turbulence intensity with relatively calm regions (A) and structures resembling turbulent spots (B) during this phase. At $\phi = 0.6$, the turbulent structures from the wake begin to destabilize the until then, laminar suction side boundary layer at the LE. Subsequently, at around $\phi = 0$, after the wake has passed, a new laminar boundary layer starts to develop from the LE until it separates. Fig. 10 underlines this argument. While the variance of c_f upstream of separation is negligible in the case without wakes, significant variance can be observed on the suction side in the case with wakes indicating a more turbulent boundary layer.

The system of secondary flows is driven by the interaction of the incoming end wall boundary layer with the blade and the passage cross flow generated by the pressure difference between pressure und suction side. This cross flow can be seen in Fig. 13 (A) represented as surface streaklines visualized using line integral convolution (LIC). The pressure side leg of the horse shoe vortex is amplified by the pressure gradient, lifts off from the end wall and becomes the passage vortex (PV) while the suction side leg rapidly dissipates. On the suction side of the blade, the PV induces a cross flow towards midspan (B), significantly reducing the channel height in which statistically 2D effects dominate the flow (C). Together with the trailing shed vortex (TSV), it forms the center of secondary flow loss [18]. Fig. 14 shows the total pressure loss coefficient ω at $x/C_{ax} = 1.4$ both time averaged and spatially averaged using the symmetry plane at $z = 0$. Note that the reference stagnation and static pressures are taken at midspan. For reference, the experiment is plotted as white contour lines over the case without wakes and shows a very good agreement over the whole plane.

The simulation with wakes shows increased total pressure loss over the complete channel height but especially in the region of the secondary flow vortices. This might seem counterintuitive at first since the wakes are able to suppress the suction side separation bubble on the blade. Still, the peak loss at midspan is increased by 20% and the mixing of the cylinder wake during its convection through the blade passage leads to an overall increased total pressure loss by a factor of 1.33 at midspan. While the shape of

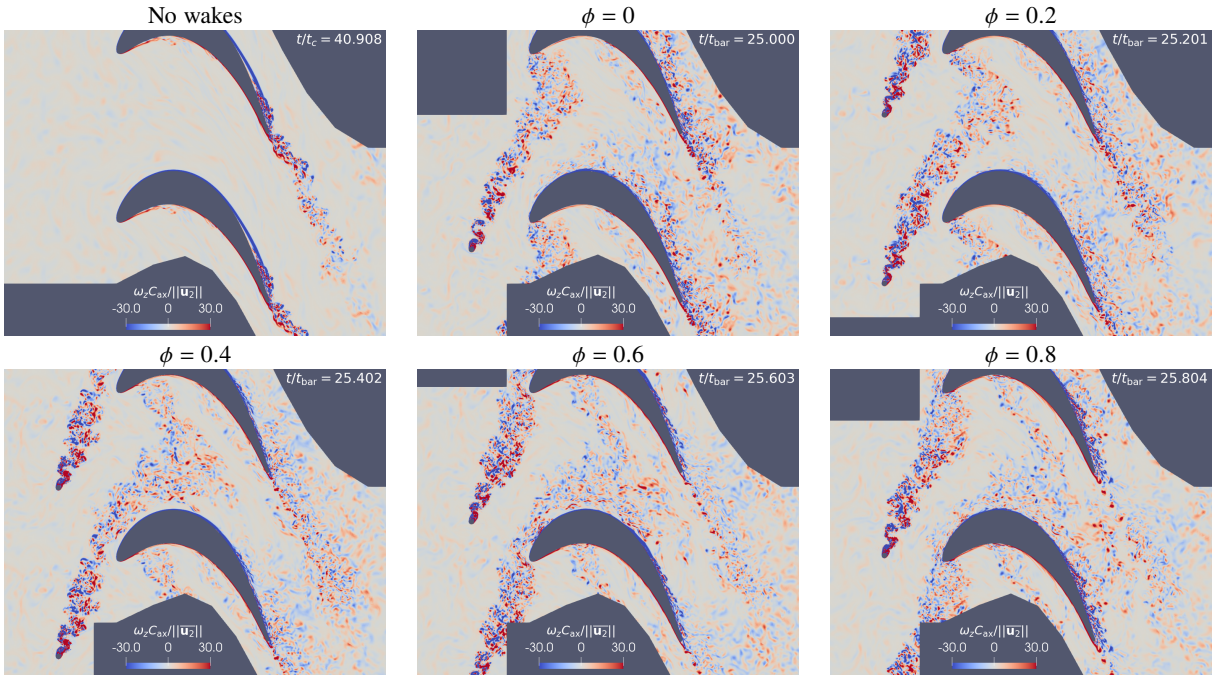

Fig. 11 Instantaneous vorticity ω_z at midspan for the case without wakes and 5 phases with wakes

the loss distribution near the end wall boundary layer seems to be essentially not influenced by the wakes, the structure of the vortex loss region changes with the losses generated by the PV becoming dominant over the losses generated by the TSV.

To understand the mechanisms behind this, we performed a Proper Orthogonal Decomposition (POD) of the flow field in the wake plane at $x/C_{ax} = 1.4$ using combined snapshots of all three fluctuating velocity components u', v' and w' [26]. This analysis revealed an essentially fully turbulent spectrum for the case without wakes with only very subtle large-scale motions of the secondary vortices accounting for 2% of the total energy in the first two modes. It cannot be ruled out by the present investigation that a very low frequency periodic oscillation of the secondary flow system exists, as e.g. reported using Particle Image Velocimetry (PIV) for compressor corner separation with a period of 80 convective time units [27]. On the other hand, in the case with wakes, the first two modes contain 21% of the total energy and, in addition to the midspan effects, exhibit a significant motion of the PV and TSV. The results are presented in Fig. 15 as a phase-averaged reconstruction of the vorticity ω_x using the first six POD modes. A comparison of the averages on the left confirms the above discussion in that the area covered by the secondary vortices is more smeared out with incoming wakes. Here, the PV can be found in red with a positive sense of rotation while the TSV rotates in the opposite direction indicated by blue colors. The phase-averaged values illustrate the large-scale motion of the vortex system caused by the wakes. Most notably, a second center of positive vorticity periodically occurs at $\phi = 0.4$ (A). At this point, the TSV is in its most smeared out state before it starts to re-establish at $\phi = 0.8$ (B) and gain its maximum strength at $\phi = 0$ (C).

To connect this analysis with the rest of the flow field, data obtained through in-situ 3D phase averages are visualized in Fig. 12. On the symmetry plane at $z = 0$, the magnitude of the velocity difference between the phase average and the time average $||\widetilde{\mathbf{u}} - \overline{\mathbf{u}}||$ is shown to indicate the position of the wake. The flow topology on the suction side surface is visible on the upper part of the blade as surface streaklines. Unfortunately, even after 50 bar passes, the phase averages are still rather noisy, which makes it especially hard to smoothly evaluate gradient quantities such as vorticity or the Q-criterion. Hence, we visualize the vortices using the Q-criterion only for the average flow field while we resort to slices of vorticity $\widetilde{\omega_x}$ at $x/C_{ax} = \{0.6, 1.0, 1.4\}$ to track the development of the passage vortex. The latter still exhibits a significant amount of noise. Qualitatively, however, the structures agree very well with Fig. 15, highlighting the usefulness of POD to extract periodic phenomena from turbulent flow fields. Already at $x/C_{ax} = 0.6$, the PV, which can again be identified on the slices as area of positive axial vorticity, shows a significant variation in size between the different phases. While the positive vorticity extends far into the passage at $\phi = 0$ (B), the PV is compressed towards the suction surface and lifted off the end wall until $\phi = 0.6$ when it starts to relax again (C). In the plane at $x/C_{ax} = 1$, the same behavior can be observed with a phase shift of roughly 0.4 (B', C'). This movement modulates the induced cross flow towards midspan in the end wall region of the blade (D). Another factor is the periodic flow separation at midspan (A). When it appears at $\phi = 0.4$, it drives more fluid from the end wall towards midspan. This influences the convergence of streaklines feeding the TSV by moving it towards midspan while at the same time weakening it (E). This can be seen in the TE plane at $x/C_{ax} = 1$ where the TSV is strongest and closest to the end wall at $\phi = 0.2$ just before the midspan flow separates. In the subsequent phases, this area of negative vorticity is driven away from the end wall and weakened until $\phi = 0$. Hence, the combined influence of the moving PV and the intermittent separation leads to the movement of the TSV making it more spread out on average compared to the case without wakes. The movement of PV and TSV can be observed in the wake plane at x/C_{ax} with a respective phase shift.

4.2 Pressure side. The physics of the pressure side separation have been represented less prominently in the literature. Fig. 16 shows the formation of vortical structures along the pressure surface in a section between $z = \pm\frac{1}{8}h$ around midspan. These structures emerge shortly behind the LE and are stretched towards trailing edge as the flow accelerates. Furthermore, long vortex streaks are visible at a distance to the wall. The origin of the vortex structures on the pressure surface has been identified in the literature as either Taylor-Görtler instabilities, in case of low freestream turbulence, or as strained wake vortices, in case of high freestream turbulence [28]. Shortly behind the LE, the shear layer on the

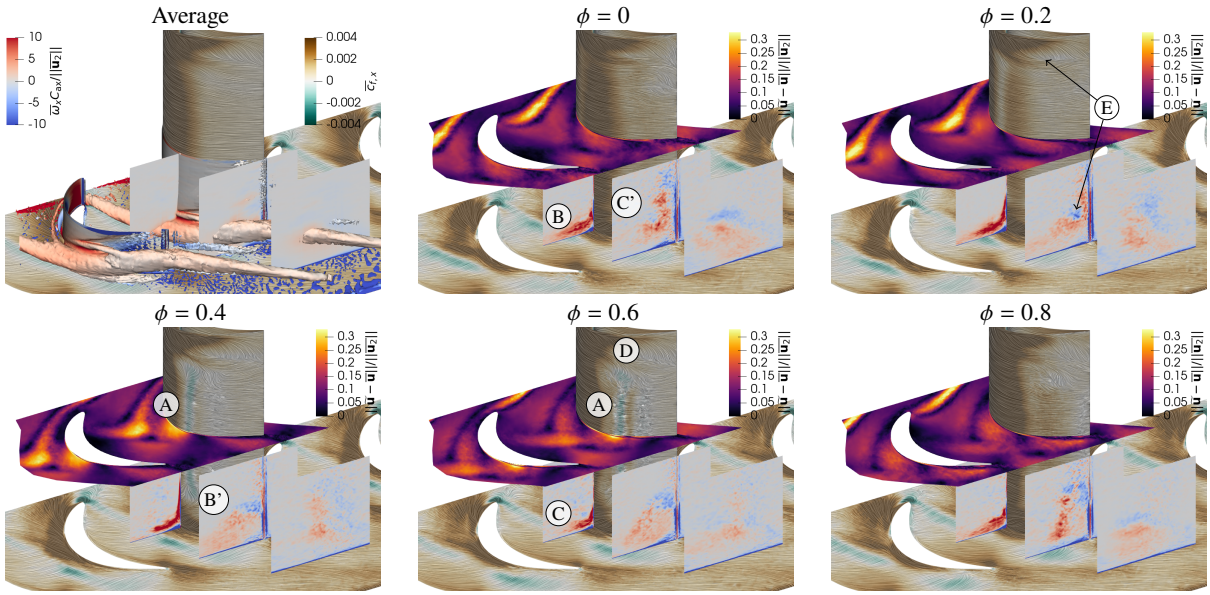

Fig. 12 Averaged and phase-averaged surface streaklines and axial vorticity ω_x in planes $x/C_{ax} = \{0.6, 1.0, 1.4\}$. Vortices of averaged solution visualized with $QC_{ax}^2/||\overline{\mathbf{u}_2}||^2 = 1$ isosurface colored with ω_x, midspan wake visualized using difference of phase-averaged and time averaged velocity $||\overline{\mathbf{u}} - \overline{\mathbf{u}}||$

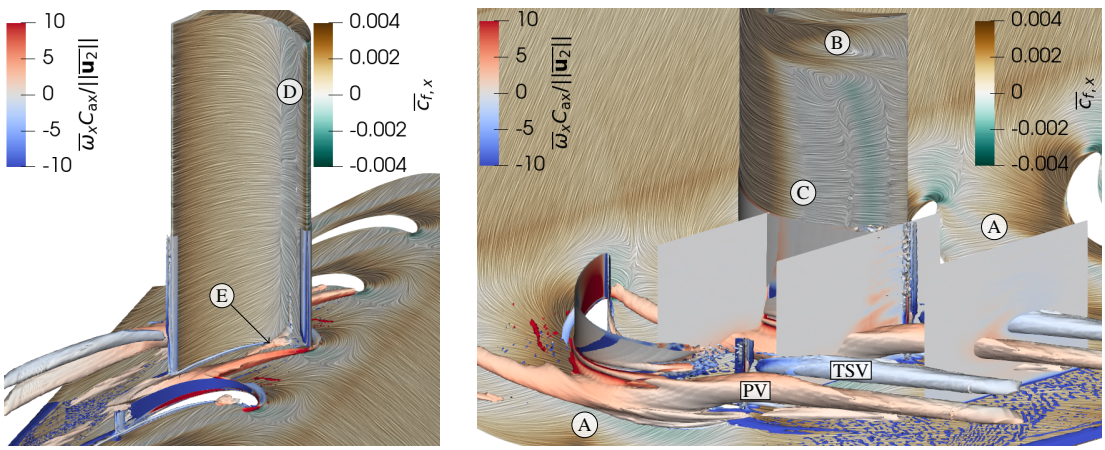

Fig. 13 Averaged surface streaklines on pressure side (*left*) and suction side (*right*) and tip wall at positive z colored with axial wall shear stress component for the case without wakes, vortices visualized using a $QC_{ax}^2/||\overline{\mathbf{u}_2}||^2 = 1$ isosurface colored with axial vorticity, axial vorticity ω_x additionally shown in planes $x/C_{ax} = \{0.6, 1.0, 1.4\}$.

pressure side lifts-off the blade wall and becomes unstable. It is, therefore, concluded that the primary instability causing the vortex structures along the pressure surface is triggered by this separation. The characteristic z-aligned roll-ups are consequently observable (1). After their formation, these roll-ups are stretched into hairpin vortices (2). Towards the trailing edge, where the flow is accelerated, the hairpin vortices tear apart, forming pairs of counter-rotating elongated structures. A comparable mechanism has been found at the Reynolds number of 200,000 albeit with much finer structures, of course [7]. An additional mechanism is observed, which causes the generation of the extremely long vortex structures at a distance to the blade surface. These structures are traced back to the LE, where structures similar to horseshoe vortices are forming from elongated vortices in the free stream (3). From here, these structures are stretched into the passage. As the vortices move along the pressure surface, they induce additional secondary flow structures, aligned with the pressure surface flow. Depending on the axial position where the elongated vortices lift off the blade surface, they are found to drift into the undisturbed passage flow.

As seen in Fig. 13 (*left*), the separation bubble also interacts with the end wall flow. Due to the diverging channel, the flow is directed towards the end walls, which has a very strong effect in the low speed regions on the pressure surface (D). Consequently, we can observe an increasing cross flow in the backflow, which lifts off the blade close to the end wall and rolls up as a vortex (E) with the same direction of rotation as the PV. It then dissipates rather quickly next to the stronger PV. The effect of the wakes on the pressure side separation was also investigated using 3D phase averages, which are not plotted here due to space constraints. Again, the separation becomes intermittent. It establishes from the end walls at $\phi = 0.6$, until the flow is fully separated across the span at $\phi = 0.8$ when wake impinges the LE. Once, the wake starts depositing turbulence in this region, both separation and reattachment point move downstream in $\phi = 0$ until the separation starts to disappear from midspan at $\phi = 0.2$ and most of the span is attached again at $\phi = 0.4$. On overage, we have backflow close to the end walls while low speed forward flow directed towards the end walls can be observed over most of the span, leading to a

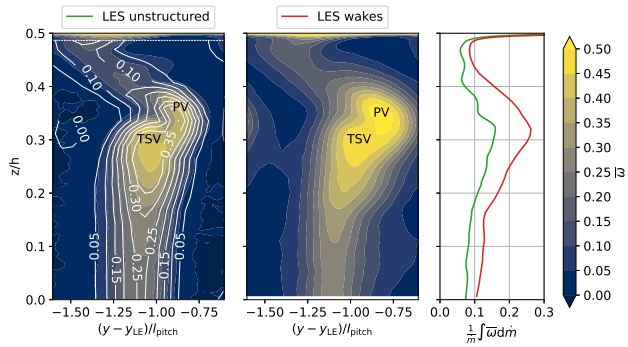

Fig. 14 Comparison of total pressure loss coefficient at $x/C_{ax} = 1.4$ spatially resolved and pitchwiss mass-averaged for the cases with and without wakes, experiment shown as white contour lines

weakening of the vortex co-rotating with the PV.

5 Conclusion

With the flow through the MTU T161 at a Reynolds number of 90,000 and a Mach number of 0.6 with and without upstream wake generators, we have presented a first 3D application of the numerical test rig based on a high-order DGSEM introduced in the first two parts of this paper. The numerical setup was briefly described and validated against numerical references and experiments based on time averaged data. In the following, the flow physics at midspan and of the complex end wall flow were discussed. The configuration with wake generators represents a purely numerical experiment. Their influence was investigated in detail showing increased total pressure losses over the whole span and periodic movement of the secondary vortex system. Nevertheless, the computational campaign produced an enormous amount of data at different temporal and spatial resolutions which we have only begun to analyze and will continue to do so with more focus on modal decomposition techniques. Furthermore, the dataset can be used as a benchmark for (U)RANS models or serve as a source for data-driven modeling. The next steps, from our perspective, are the extension of the numerical test rig to rotational configurations to be able to investigate blade row interactions using real blade geometries in realistic environments.

Acknowledgment

We gratefully acknowledge Marco Rosenzweig for the fruitful discussions and for making available his most recent results for comparison. Furthermore, we thank Nima Fard Afshar for making his data digitally available.

Nomenclature

Roman letters

C = chord length [m]
c_f = skin friction coefficient
h = local channel height [m]
l = length [m]
$\dot{m}$ = mass flow [kg/s]
n = number of elements
N = polynomial order
p = pressure [Pa]
s = surface length from leading edge [m]
t = time [s]
$\mathbf{u}$ = velocity vector [m/s]
u, v, w = Cartesian velocity components [m/s]

Greek letters

α = angle with respect to axial direction
δ_{99} = 99% boundary layer thickness [m]
$\Delta\xi, \Delta\eta, \Delta\zeta$ = streamwise, wall-normal, spanwise solution point distances [m]
ϕ = phase between bar and blade, t mod t_{bar}
Φ = flow coefficient
ρ = density [kg/m^3]
τ_w = wall shear stress vector [Pa]
θ = boundary layer momentum thickness [m]
ω = vorticity vector [s^{-1}]
ω = total pressure loss coefficient

Dimensionless groups

Re = Reynolds number
Ma = Mach number
Sr = Strouhal number
nDoF = number of degrees of freedom

Superscripts and subscripts

1 = upstream value
2 = downstream value
area = area averaged over panel
avg = average
ax = axial component
c = convection through blade passage
LE = leading edge value
ref = reference value
th = value based on isentropic relations
t = stagnation value
$\square^+$ = wall units
$\overline{\square}$ = time averaged value
$\square'$ = fluctuating value, $\square - \overline{\square}$
$\widetilde{\square}$ = phase-averaged value

References

[1] Gbadebo, S. A., Cumpsty, N. A., and Hynes, T. P., 2005, "Three-Dimensional Separations in Axial Compressors," J. Turbomach., **127**(2), pp. 331–339.
[2] Taylor, J. V. and Miller, R. J., 2016, "Competing Three-Dimensional Mechanisms in Compressor Flows," J. Turbomach., **139**(2), 021009.
[3] Langston, L., 2001, "Secondary Flows in Axial Turbines—A Review," Ann. New York Acad. Sci., **934**(1), pp. 11–26.
[4] Cui, J., Nagabhushana Rao, V., and Tucker, P., 2015, "Numerical Investigation of Contrasting Flow Physics in Different Zones of a High-Lift Low-Pressure Turbine Blade," J. Turbomach., **138**(1), 011003.
[5] Koschichow, D., Ciorciari, R., Fröhlich, J., and Niehuis, R., 2015, "Analysis of the influence of periodic passing wakes on the secondary flow near the endwall of a linear LPT cascade using DNS and U-RANS," *Proceedings of the 11th European Conference on Turbomachinery Fluid Dynamics and Thermodynamics*, Madrid, Spain.
[6] Pichler, R., Zhao, Y., Sandberg, R., Michelassi, V., Pacciani, R., Marconcini, M., and Arnone, A., 2019, "Large-Eddy Simulation and RANS Analysis of the End-Wall Flow in a Linear Low-Pressure Turbine Cascade, Part I: Flow and Secondary Vorticity Fields Under Varying Inlet Condition," J. Turbomach., **141**(12), 121005.
[7] Iyer, A., Abe, Y., Vermeire, B., Bechlars, P., Baier, R., Jameson, A., Witherden, F., and Vincent, P., 2021, "High-order accurate direct numerical simulation of flow over a MTU-T161 low pressure turbine blade," Comput. Fluids, **226**, p. 104989.
[8] Donovan, M. H., Rumpfkeil, M. P., Marks, C. R., Robison, Z., and Gross, A., 2022, "Low Reynolds Number Effects on the Endwall Flow Field in a High-Lift Turbine Passage," J. Turbomach., **145**(3), 031006.
[9] Robison, Z. and Gross, A., 2021, "Large-Eddy Simulation of Low-Pressure Turbine Cascade with Unsteady Wakes," Aerospace, **8**(7).
[10] Robison, Z. and Gross, A., 2022, "Comparative numerical investigation of wake effect on low-pressure turbine endwall flow," Aerosp. Sci. Technol., **131**, p. 107970.
[11] Floryan, J. M., 1986, "Görtler instability of boundary layers over concave and convex walls," Phys. Fluids, **29**(8), pp. 2380–2387.
[12] Gross, A., Marks, C. R., Sondergaard, R., Bear, P. S., and Mitch Wolff, J., 2018, "Experimental and Numerical Characterization of Flow Through Highly Loaded Low-Pressure Turbine Cascade," J. Propul. Power, **34**(1), pp. 27–39.
[13] Gier, J., Raab, I., Schröder, T., Hübner, N., Franke, M., Kennepohl, F., Lippl, F., Germain, T., and Enghardt, L., 2007, "Preparation of Aero Technology for new Generation Aircraft Engine LP Turbines," *1st CEAS European Air and Space Conference*, Berlin, Germany.

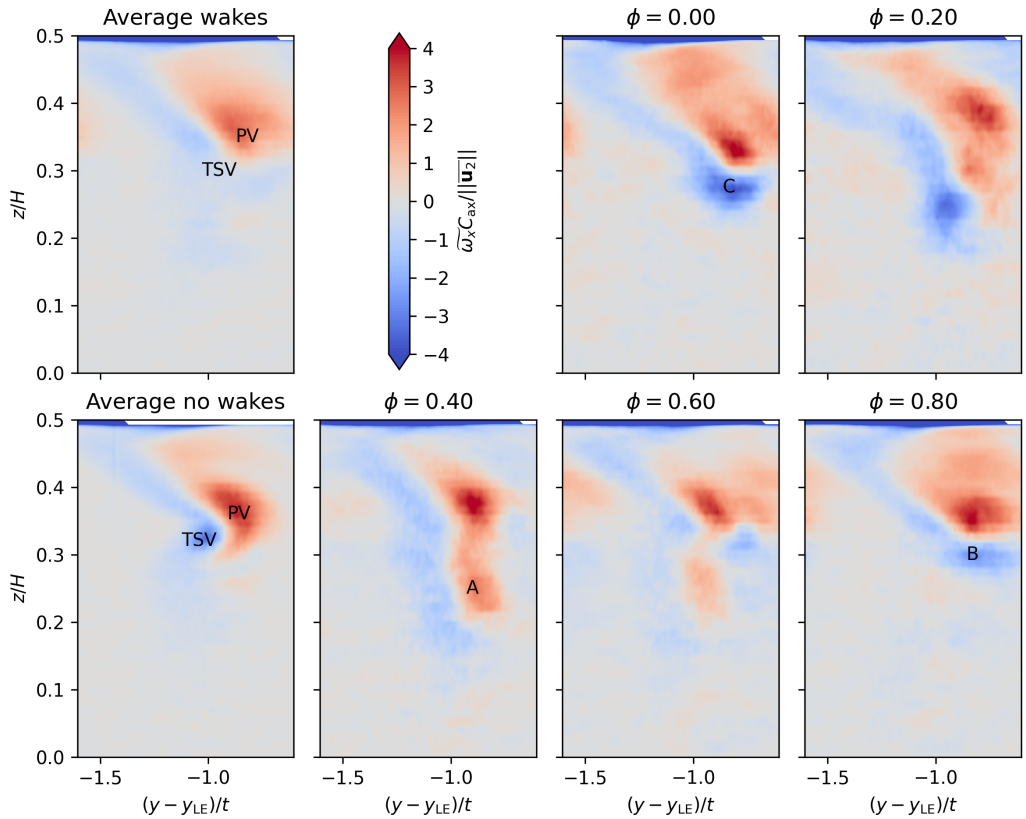

Fig. 15 Phase averaged vorticity $\widetilde{\omega_x}$ at $x/C_{ax} = 1.4$ reconstructed from 6 POD modes compared with time averages with and without wakes

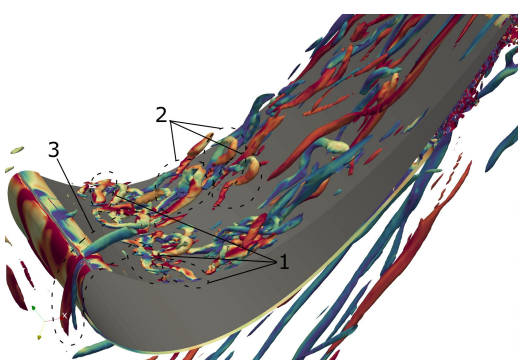

Fig. 16 Instantaneous vortex structures on the pressure side around midspan visualized using a $Q C_{ax}^2/||\overline{\mathbf{u_2}}||^2 = 10$ isosurface colored with streamwise vorticity

[14] Müller-Schindewolffs, C., Baier, R.-D., Seume, J. R., and Herbst, F., 2017, "Direct Numerical Simulation Based Analysis of RANS Predictions of a Low-Pressure Turbine Cascade," J. Turbomach., **139**(8), 081006.

[15] Fard Afshar, N., Deutsch, J., Henninger, S., Kozulovic, D., and Bechlars, P., 2022, "Turbulence Anisotropy Analysis at the Middle Section of a Highly Loaded3D Linear Turbine Cascade Using Large Eddy Simulation," *Proceedings of Global Power and Propulsion Society*, Chania, Greece.

[16] Bergmann, M., Gölden, R., and Morsbach, C., 2018, "Numerical investigation of split form nodal discontinuous Galerkin schemes for the implicit LES of a turbulence channel flow," 7th European Conference on Computational Fluid Dynamics.

[17] Bergmann, M., Morsbach, C., and Ashcroft, G., 2020, "Assessment of Split Form Nodal Discontinuous Galerkin Schemes for the LES of a Low Pressure Turbine Profile," *Direct and Large Eddy Simulation XII*, M. García-Villalba, H. Kuerten, and M. V. Salvetti, eds., Springer International Publishing, Cham, pp. 365–371.

[18] Morsbach, C., Bergmann, M., Tosun, A., Kügeler, E., and Franke, M., 2022, "Large eddy simulation of a low pressure turbine cascade with turbulent end wall boundary layers," *DLES13 - Direct and Large Eddy Simulation*, Udine, Italy, doi: 10.48550/arXiv.2212.08432.

[19] Martinstetter, M., Niehuis, R., and Franke, M., 2010, "Passive Boundary Layer Control on a Highly Loaded Low Pressure Turbine Cascade," *Turbo Expo: Power for Land, Sea, and Air*, Vol. Volume 7: Turbomachinery, Parts A, B, and C, pp. 1315–1326, doi: 10.1115/GT2010-22739.

[20] Rosenzweig, M., Kozul, M., Sandberg, R., R., P., and Marconcini, M., 2023, "High-Fidelity Simulations and RANS Analysis of a Low-Pressure Turbine Cascade in a Spanwise-Diverging Gas Path - End-Wall Flow Analysis and Loss Generation Mechanisms," *Proceedings of ASME Turbo Expo 2023: Turbomachinery Technical Conference and Exposition*, Boston, MA, USA, Paper No. GT2023-101039.

[21] Shur, M. L., Spalart, P. R., Strelets, M. K., and Travin, A. K., 2014, "Synthetic Turbulence Generators for RANS-LES Interfaces in Zonal Simulations of Aerodynamic and Aeroacoustic Problems," Flow Turbul. Combus., **93**(1), pp. 63–92.

[22] Bergmann, M., Morsbach, C., Ashcroft, G., and Kügeler, E., 2021, "Statistical Error Estimation Methods for Engineering-Relevant Quantities From Scale-Resolving Simulations," J. Turbomach., **144**(3), 031005.

[23] Geuzaine, C. and Remacle, J.-F., 2009, "Gmsh: A 3-D finite element mesh generator with built-in pre- and post-processing facilities," Int. J. Numer. Methods Engrg., **79**(11), pp. 1309–1331.

[24] Morsbach, C. and Bergmann, M., 2020, "Critical Analysis of the Numeri-

cal Setup for the Large-Eddy Simulation of the Low-Pressure Turbine Profile T106C," *Direct and Large Eddy Simulation XII*, M. García-Villalba, H. Kuerten, and M. V. Salvetti, eds., Springer International Publishing, Cham, pp. 343–348.

[25] Schlatter, P. and Örlü, R., 2010, "Assessment of direct numerical simulation data of turbulent boundary layers," J. Fluid Mech., **659**, p. 116–126.

[26] Weiss, J., 2019, *A Tutorial on the Proper Orthogonal Decomposition*.

[27] Dawkins, I., Taylor, J., Ottavy, X., and Miller, R., 2022, "The Unsteady Topology of Corner Separations," J. Turbomach., **144**(11), 111001.

[28] Cui, J., Nagabhushana Rao, V., and Tucker, P., 2017, "Numerical investigation of secondary flows in a high-lift low pressure turbine," Int J Heat Fluid Fl, **63**, pp. 149–157.

List of Figures

List of Tables